ORIGINAL RESEARCH ARTICLE

Eulerian–Lagrangian Numerical Simulation of Powder Bed Denudation and Spatter Behavior During Powder Bed Fusion Process

LIU CAO, RUI-FAN MENG, QIN-DAN ZHANG, and ZHEN-ZHEN GUI

Powder bed fusion using a laser beam (PBF-LB) is rapidly developing toward high laser power, high scanning speed, and multiple lasers; however, spatter has become one of the major bottlenecks limiting PBF-LB to form large metal parts. In this paper, the Eulerian–Lagrangian numerical simulation study was carried out for the spatter formation and spatter-protective gas flow coupling behavior. Among them, the Eulerian model considered the effect of particles on the gas-phase flow, and the Lagrangian model took into account the fluid drag force, gravity, buoyancy, non-uniform pressure distribution, additional mass force, and particle–particle collisions. For the effect of metal vapor on spatter and powder bed denudation, it was found that the larger the metal vapor jet speed or jet area, the faster the spatter speed and the larger the width of the powder bed denudation zone; the larger the lateral dimension of the metal vapor action zone (the scanning direction is longitudinal), the larger the number of spatters. For the effect of protective gas flow velocity on spatter movement, it was found that the longitudinal movement distance of spatter was significantly larger for larger protective gas flow velocity, and almost all spatters fell on the powder bed or substrate for smaller protective gas flow velocity. This paper is expected to provide scientific guidance for regulating PBF-LB spatter.

https://doi.org/10.1007/s11661-023-07055-3
© The Minerals, Metals & Materials Society and ASM International 2023

I. INTRODUCTION

POWDER bed fusion using a laser beam (PBF-LB), one of the most promising technologies for rapid forming of large metal parts, is rapidly developing toward high laser power, high scanning speed, and multiple lasers.[1] However, the complex interaction between the laser beam and the metal powder during the forming makes spatter accompany the whole PBF-LB process. Spatter has become one of the major bottlenecks in PBF-LB forming of large metal parts, as it leads to porosity and inclusion defects on the one hand[2] and reduces the quality of powder recovery on the other.[3]

In the PBF-LB forming process, on the one hand, the evolutionary behavior of spatter is closely related to the complex kinetic phenomena occurring in the molten pool. That is, the metal material evaporates violently under the action of high energy density, the high-temperature molten pool forms the keyhole driven by the strong recoil pressure of metal vapor, and there is a complex mutual mechanical interaction between the keyhole, molten pool, and metal vapor. The high-speed jet of metal vapor causes violent fluctuations on the molten pool, causing some of the liquid–metal to be ejected with the metal vapor, forming the so-called droplet spatter.[4] On the other hand, the evolutionary behavior of spatter is significantly influenced by powder bed denudation. That is, under the combined influence of the protective gas as well as the metal vapor injected at high speed, gas convection is induced near the laser action zone based on the Bernoulli effect, resulting in the accumulation of metal particles in the laser action zone. Powder bed denudation causes some of the metal particles to enter the laser action zone, which is then heated into the molten pool or ejected with the metal vapor, forming the so-called powder spatter.[5] Figure 1 shows the schematic diagram of powder bed denudation and spatter behaviors during PBF-LB forming process.

Conducting experimental studies on the characteristics observation and process laws of powder bed denudation and spatter is the basis for understanding the PBF-LB spatter behavior. At present, with the help of high-speed cameras,[6] X-ray *in situ* imaging,[7] acoustic information acquisition,[8] and other experimental means, researchers have focused on the effects of laser

LIU CAO, RUI-FAN MENG, QIN-DAN ZHANG, and ZHEN-ZHEN GUI are with the Institute for Systems Rheology, School of Mechanical and Electrical Engineering, Guangzhou University, Guangzhou 510006, Guangdong, P.R. China. Contact e-mail: caoliu@gzhu.edu.cn.
Manuscript submitted August 30, 2022; accepted April 3, 2023.
Article published online May 3, 2023

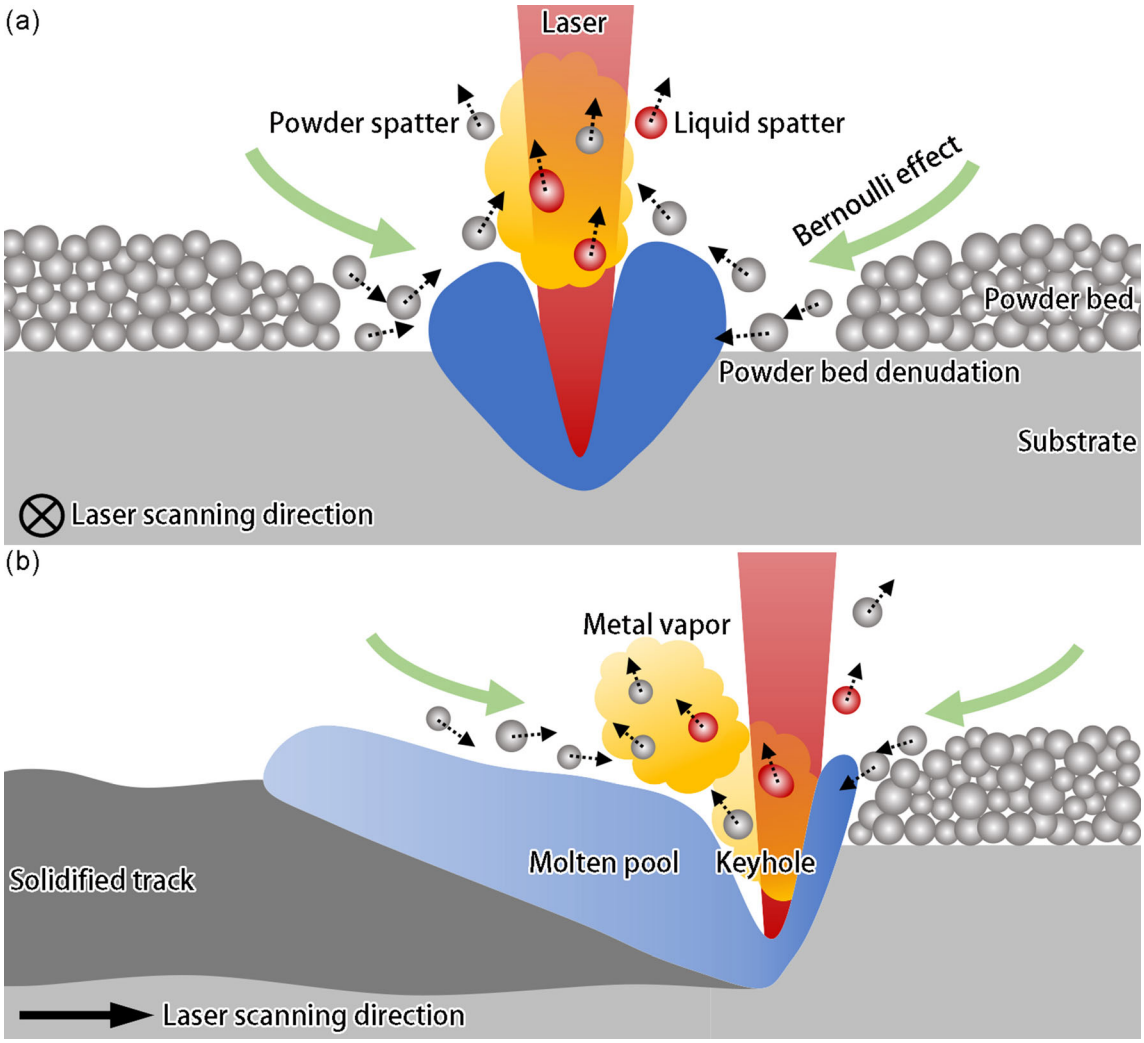

Fig. 1—Schematic diagram of powder bed denudation and spatter behaviors during PBF-LB forming process: (*a*) view perpendicular to the scanning direction; (*b*) view parallel to the scanning direction.

power,[9] scanning speed,[9] multiple lasers,[9] powder bed thickness,[10] protective gas type,[11] protective gas pressure,[12] protective gas flow rate,[13] and other factors on powder bed denudation and spatter behaviors. Qu *et al.*[14] proposed to reduce the large droplet spatter of PBF-LB with the help of nanoparticles. The regulation mechanism includes two aspects, firstly, nanoparticles attenuate the fluctuation of the molten pool and secondly, nanoparticles attenuate the aggregation of droplets. The above experimental studies have played an important role in the in-depth understanding of powder bed denudation and spatter behaviors. However, because the PBF-LB-forming process occurs in a rapidly changing solid–liquid-gas coupling environment, where the complex thermophysical interaction process often occurs in microsecond time, and the metal vapor is high in temperature, low in density, and invisible to the naked eye, the existing experimental means are insufficient to capture the information of metal vapor temperature and velocity in the keyhole, which makes it difficult to quantify and visualize the influence of metal vapor and protective gas on powder bed denudation and spatter behaviors.

Based on the obtained experimental research results, the research on the prediction of powder bed denudation and spatter behaviors can provide a new path to reveal the evolution law and regulation mechanism of PBF-LB spatter. Eulerian–Lagrangian method[15] is a class of numerical simulations specifically designed to analyze the coupling behavior of fluid and particle phases. At present, researchers mainly rely on Eulerian–Lagrangian method to predict powder bed denudation and spatter behaviors, and some of the current researches are given in Table I. In summary, the current simulation studies fall into two main categories, one focusing on the formation of powder bed denudation and spatter, when the motion of the particles under the action of metal vapor and the coupling between the particles and the gas phase are considered, but the spatter motion inside the forming cavity after spatter formation is not predicted.[16,17,19] The other focuses on the spatter movement in the forming cavity after spatter formation, when the drag effect of the protective gas on

Table I. Progress in the Prediction of Powder Bed Denudation and Spatter Behaviors by Means of Eulerian–Lagrangian Method

Simulation Methods	Commercial Software or Open-Source Codes	Realized Contents	Simplified or Unrealized Contents	Research Institutions and References
CFD-DEM				
	unknown	predicted the powder bed denudation and spatter behaviors, considered the coupling between the particle phase and the fluid phase, and obtained the velocity and temperature distributions of particles	did not take into account the melting and solidification of metal particles, artificially specified the incident rate, direction and temperature of the metal vapor, and limited the prediction area	National University of Singapore [16,17]
	fluent + EDEM	predicted the forming cavity flow field and spatter motion	did not calculate the temperature field, artificially specified the initial velocity of particles, did not consider the metal vapor, and did not consider the effect of particles on the gas-phase flow field	National Cheng Kung University [18]
	CFDEM, *i.e.,* OpenFOAM + LIGGGHTS	predicted the melting and solidification of metal particles, and predicted the motion of particles and their surrounding flow field	did not consider the metal vapor, and limited the prediction area	Hong Kong University of Science and Technology [19]
CFD-DPM				
	fluent	predicted the forming cavity flow field and spatter motion, and considered the coupling between the particle phase and the fluid phase	did not calculate the temperature field, artificially specified the initial velocity of particles, and did not consider the metal vapor	Robert Bosch LLC [20] Nanyang Technological University [21]
CFD-Lagrangian method	STAR-CCM +	predicted the melting, gasification and solidification of metal particles, and predicted the powder spatter	The control algorithm for particle motion is very simple, and did not consider the effect of particles on the gas-phase flow field	Access e.V. [22]

(CFD: Computational Fluid Dynamics; DEM: Discrete Element Method; DPM: Discrete Particle Method).

the metal particles is considered, but the initial velocity of the particles is often directly specified without predicting the formation of powder bed denudation and spatter.[18,21,22] It can be seen that it is necessary to predict both the formation of powder bed denudation and spatter and the subsequent motion of spatter in the forming cavity, for obtaining the complete motion trajectory of spatter.

This paper conducts a numerical simulation study of the powder bed denudation and spatter behaviors of PBF-LB based on the open-source computational fluid dynamics code OpenFOAM. Among them, the spatter formation and spatter-protection gas flow coupling behavior are predicted. In this paper, the effects of metal vapor injection velocity and injection area on the spatter formation and powder bed denudation, as well as the effects of protective gas flow velocity on spatter motion are investigated separately. This paper is expected to provide scientific guidance for the regulation of spatter.

II. EULERIAN–LAGRANGIAN NUMERICAL MODEL

The main objective of this paper is to reproduce the powder bed denudation and spatter formation, as well as the spatter trajectory under the action of protective gas. Numerical simulations in the absolute sense need to fully reproduce the melting, vaporization, and solidification of metal particles under the action of laser, the powder bed denudation and spatter formation in the mesoscopic molten pool scale, and the spatter trajectory in the macroscopic forming cavity scale. This work is a typical multiphase (solid phase, liquid phase, gas phase, particle phase), multiphysical field (thermal field, flow field), and multiscale (mesoscopic, macroscopic) simulation study, which is difficult to carry out directly at present. In addition, experimental studies have found that powder spatter accounts for up to 85 pct of the total spatter.[4] Therefore, the numerical simulation study here was carried out based on the following simplifications and assumptions:

1. Only powder spatter is considered, and melting, vaporization, and solidification of metal particles under the laser action are not calculated, and a high-speed inlet boundary is imposed below the powder bed in lieu of metal vapor, and the inlet velocity is set according to experiment.
2. Only the flow field is calculated, and the temperature field is not calculated.
3. The difference in composition between metal vapor and protective gas is not distinguished, and both are considered as the same fluid phase in the calculation, and the fluid phase is considered as incompressible Newtonian fluid.
4. It is considered that all metal particles are ideally spherical.

A. *Computational Fluid Dynamics for Fluid Phase*

In this paper, the single-phase Navier–Stokes equation is used to describe the motion of the fluid phase, the effect of particles on the fluid-phase flow is considered, and the turbulence model is applied. The momentum equation and continuity equation used here are shown below:

$$\frac{\partial \rho_f u_f}{\partial t} + \nabla \cdot \left(\rho_f \vec{u}_f \otimes \vec{u}_f\right) = -\nabla p_f + \mu_f\left(\nabla \vec{u} + \nabla \vec{u}^T\right) + \nabla \cdot \bar{\bar{\tau}}_{sgs} + \rho_f \vec{g} + \vec{f}_{p-f} \quad [1]$$

$$\nabla \cdot \underset{f}{\vec{u}} = 0 \quad [2]$$

where ρ_f is the density of the fluid phase, kg/m^3; $\vec{u}$ is the velocity of the fluid phase, m/s; t is the time, s; p_f is the pressure of the fluid phase, Pa; μ_f is the dynamic viscosity of the fluid phase, Pa·s; $\bar{\bar{\tau}}_{sgs}$ is the sub-grid stress tensor obtained by introducing the LES turbulence model;[23] $\vec{g}$ is the gravity acceleration, m/s^2; $\underset{p-f}{\vec{f}}$ is the force of particles on the fluid, N/m^3.

B. *Discrete Parcel Method for Particle Phase*

In this paper, the discrete parcel method (DPM) is used to describe the motion of metal particles, considering the effects of fluid drag force, gravity, buoyancy, non-uniform pressure distribution, particle–particle collision, and additional mass force on the particle motion. The main difference between DPM and discrete element method (DEM) is that the object of study of DPM is particle parcels, and each particle parcel can contain several particles with the same size, velocity, and other properties, and DPM can only deal with spherical particles. When the number of particles inside the particle parcel in DPM is one, it is essentially the same as the effect of DEM processing spherical particles. The particle motion control equation used here is:

$$m_p \frac{d\vec{u}_p}{dt} = \underset{f-p}{\vec{F}} + \underset{g}{\vec{F}} + \underset{p}{\vec{F}} + \underset{a}{\vec{F}} + \sum\left(\underset{n}{\vec{F}} + \underset{t}{\vec{F}}\right) \quad [3]$$

$$I_{\mathrm{p}} \frac{\mathrm{d}\vec{\omega}_{\mathrm{p}}}{\mathrm{d}t} = \sum \vec{R} \times \underset{\mathrm{t}}{\vec{F}} \quad [4]$$

in which:

$$\underset{g}{\vec{F}} = m_p \vec{g}\left(1 - \frac{\rho_f}{\rho_p}\right) \quad [5]$$

$$\underset{p}{\vec{F}} = -\frac{\pi D_p^3}{6}\nabla p_f \quad [6]$$

$$\vec{F}_a = \frac{\pi \rho_f D_p^3}{12}\left(\frac{D\vec{u}_f}{Dt} - \frac{d\vec{u}_p}{dt}\right) \quad [7]$$

where, m_p is the particle mass, kg; $\vec{u}_p$ is the particle velocity, m/s; $\vec{F}_{f-p}$ is the drag force of the fluid on particles, N; $\vec{F}_g$ is the sum of the gravitational and buoyant forces on the particle, N; $\vec{F}_p$ characterizes the effect of non-uniform pressure distribution on particle motion, N; $\vec{F}_a$ is the additional mass force, *i.e.,* the reaction force of the nearby fluid on the particle when the particle does accelerated motion, N;

F_n and F_t are the normal and tangential forces generated during the particle–particle collision, respectively, and are described here using the soft sphere model, N;[24] I_p is the rotational inertia of the particle, kg·m^2; $\vec{\omega}_p$ is the rotational angular velocity of the particle, rad/s; $\vec{R}$ is the rotation force arm, m; ρ_p is the density of the particle phase, kg/m^3; D_p is the particle diameter, m.

C. *Eulerian–Lagrangian Coupling Strategy and Simulation Process*

In the Eulerian–Lagrangian approach of this paper, the coupling between the fluid phase and the particle phase is represented by $\vec{f}_{p-f}$ in Eq. (1) and $\vec{F}_{f-p}$ in Eq. (3), respectively.The specific formulas for $\vec{f}_{p-f}$ and $\vec{F}_{f-p}$ are as follows:

$$\vec{f}_{\mathrm{p-f}} = -\frac{\sum \vec{F}_{\mathrm{f-p}}}{V_{\mathrm{cell}}} \quad [8]$$

$$\vec{F}_{\mathrm{f-p}} = \frac{\pi \rho_{\mathrm{f}} \mathrm{C_d} \mathrm{D_p^2}}{8}\left(\vec{u}_{\mathrm{f}} - \vec{u}_{\mathrm{p}}\right)\left|\vec{u}_{\mathrm{f}} - \vec{u}_{\mathrm{p}}\right| \quad [9]$$

$$\mathrm{C_d} = \begin{cases} \frac{24}{\mathrm{Re_p}}\left(1 + \frac{\mathrm{Re_p^{2/3}}}{6}\right) & \text{if } \mathrm{Re_p} \le 1000 \\ 0.424 & \text{if } \mathrm{Re_p} > 1000 \end{cases} \quad [10]$$

$$\mathrm{Re_p} = \frac{\rho_{\mathrm{f}} \mathrm{D_p}\left|\vec{u}_{\mathrm{f}} - \vec{u}_{\mathrm{p}}\right|}{\mu_{\mathrm{f}}} \quad [11]$$

where V_{cell} is the volume of a single mesh cell in the CFD calculation, m^3; C_d is the drag force coefficient;[25] Re_p is the particle Reynolds number.

The simulation study in this paper is based on the open-source CFD code OpenFOAM,[23] and Figure 2 shows the simulation flow of Eulerian–Lagrangian method here. In which, the Eulerian method is used to obtain the flow field distribution of the fluid phase and the Lagrangian method is used to obtain the motion trajectory of the particle phase. After solving each time step, the coupling force between the fluid phase and the particle phase is updated for the next time step based on the current flow field information and the particle motion information.

III. RESULTS AND DISCUSSION

A. *Spatter Formation and Powder Bed Denudation*

In this paper, we first focus on the spatter formation and powder bed denudation under the action of high-speed metal vapor. The metal material is 316L stainless steel particles, the protective gas is nitrogen, and Table II shows the parameters required for the calculation.[16,18] The initial positions of the particles were obtained with the help of the open-source discrete element method code Yade,[25] and the total calculation time was 0.1 s. The mesh size has a large impact on the accuracy of the Eulerian–Lagrangian coupling calculation, and Ref[26] . suggests that for the non-resolved Eulerian–Lagrangian coupling calculation, the mesh size should be taken as two to four times the average particle diameter, so the mesh size used here was 90 μm. In addition, the computing resources used are configured with Intel Xeon Gold 6240 CPU (dual CPU, 72 threads, 128 GB RAM) and Intel Xeon Gold 5120 CPU (dual CPU, 56 threads, 96 GB RAM). To analyze the effects of metal vapor injection velocity and size on spatter formation and powder bed denudation, simulation studies were carried out as shown in Table III.

The gas-phase flow velocity and 3D spatter distribution at different moments for the case of calculation scheme A2 are given in Figure 3. From the calculation results, it can be seen that when the high-speed gas inlet boundary came into play, a high-speed gas flow jet zone immediately appeared in the forming cavity, and it moved continuously along the scanning direction [Figures 3(a1) through (a4)]. At the same time, metal particles were continuously ejected upward under the drag effect of high-speed gas flow, forming spatters, and the generated spatters gradually increased due to the continuous movement of the high-speed gas flow jet zone [Figures 3(b1) through (b4)]. To investigate the origin of the spatter, the gas-phase and particle velocity distributions at a given moment for calculation scheme A2 are given in Figure 4. From the direction of gas-phase flow in the X-directional cross-section [Figure 4(a)], it can be seen that the gas directly above the inlet was influenced by the high-speed gas flow upward and fast, resulting in a decrease in gas pressure directly above the inlet, which makes the gas around the inlet gather in the jet zone under Bernoulli effect, and the gas flow gathered in the jet zone then drove the particles around the inlet to gradually gather in the jet zone [Figure 4(c)], which is the so-called powder bed denudation phenomenon. As can be seen, the spatters in

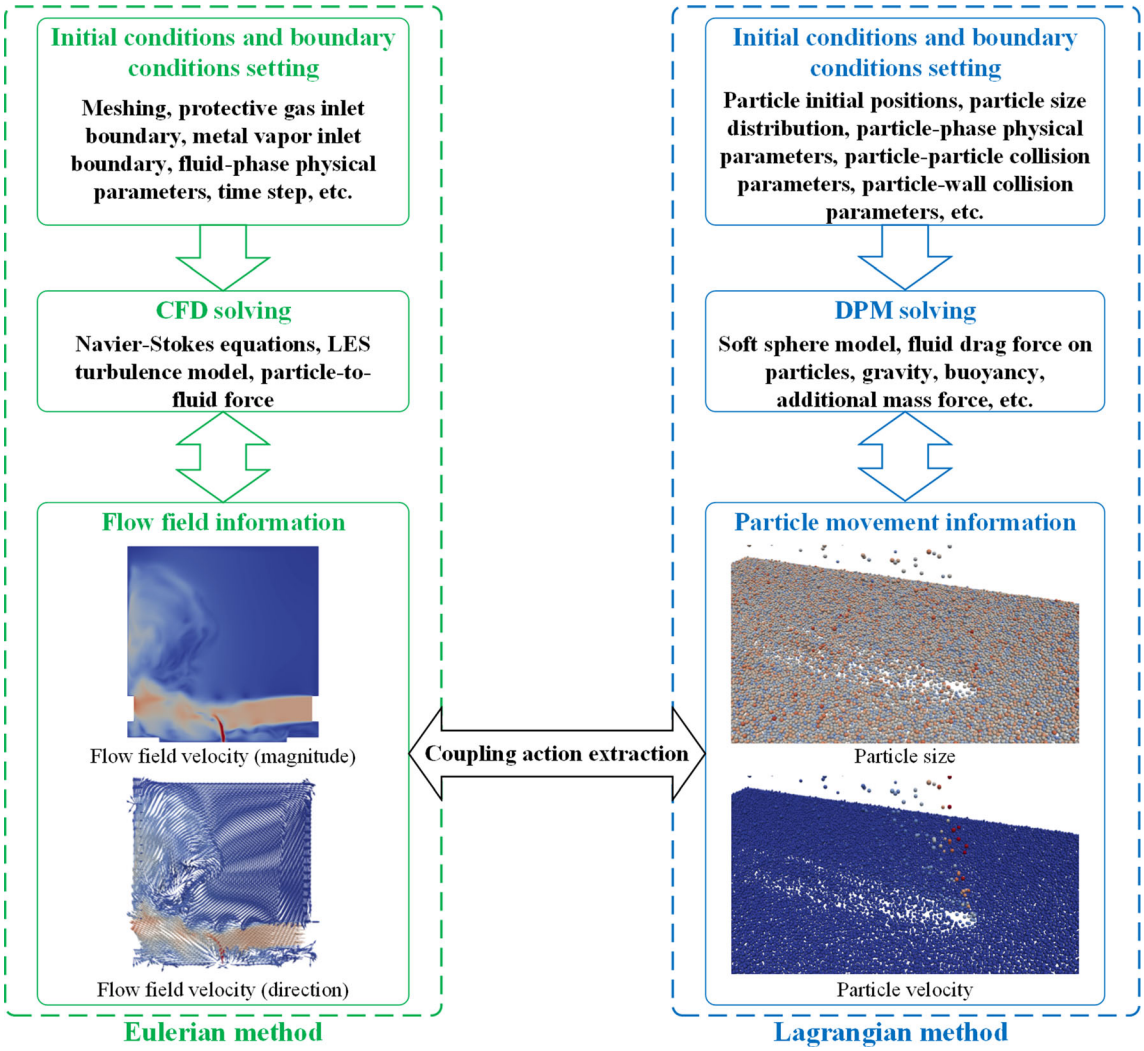

Fig. 2—Eulerian–Lagrangian method simulation flow.

Figure 4(b) originate from particles originally located above the scanning path on the one hand, and from surrounding particles that accumulate in the gas jet zone due to powder bed denudation on the other hand. The simulation results of spatter and powder bed denudation for calculation scheme A2 and the experimental results in the literature are presented in Figure 5. The qualitative comparison shows that the simulations of spatter and powder bed denudation agree well with the experimental results, so it can be concluded that the Eulerian–Lagrangian simulation method used herein can be used to reproduce the powder bed denudation and spatter behaviors in the PBF-LB forming process.

Figures 6, 7, and 8 give the calculated results for different cases of high-speed inlet velocity and size. To illustrate the effect of different inlet velocities and sizes on the high-speed gas flow jet zone, the equivalent surface with gas-phase rate of 1 m/s (Figure 6) at a certain moment for different calculation schemes is extracted here, and the rate equivalence surface is considered to represent the size of the high-speed gas flow jet zone. From the comparison results, it can be seen that when the inlet size was certain, the high-speed gas flow jet zone became significantly larger as the inlet speed gradually increased, especially its Z-directional size [Figure 6(a) through (c)]. When the inlet velocity was fixed and the X-directional size of the inlet was increased, the jet zone became significantly larger [Figures 6(b), (d)]; when the Y-directional size of the inlet was increased, the jet zone also became significantly larger [Figures 6(b), (e)]; when the X-directional and Y-directional sizes of the inlet were increased simultaneously, the jet zone became most significantly larger [Figures 6(b), (f)]. The variation of the high-speed jet zone directly affects the formation of spatter. Figures 8(a) through (c) quantifies and compares the spatter data at a certain moment for different calculation schemes, and it should be noted that the metal particles are judged to be spatter based on whether their rate is greater than 0.1 m/s. From the quantified comparison results, it can be seen that when the inlet velocity or inlet area was larger, the spatter speed was significantly faster [Figure 8(a)]; when the Y-directional size of the inlet increased, the number of spatters

Table II. Parameters Required for the Calculation[16,18]

Parameter	Value	Unit
Metal Density[16]	7800	kg/m^3
Metal Young's Modulus[16]	2.2×10^9	Pa
Metal Poisson's Ratio[16]	0.3	N/A
Protective Gas Density[18]	1.17	kg/m^3
Protective Gas Dynamic Viscosity[18]	1.18×10^{-5}	Pa·s
Gravity Acceleration	(0, 0, -9.81)	m/s^2
Particle Diameter	25 ~ 55	μm
Particle–Particle Collision		
Response coefficient	0.95	N/A
Spring coefficient	1.5	N/A
Friction coefficient[16]	0.62	N/A
Particle–Wall Collision		
Response coefficient	0.31	N/A
Spring coefficient	1.5	N/A
Friction coefficient[16]	0.62	N/A
Powder Bed Sizes	10,000 × 5000 × 100	μm
Number of Metal Particles	39,839	N/A
Scanning Speed	0.2	m/s
Scanning Length (X-direction)	8	mm
Time Step	5×10^{-6}	s
Moment when High-Speed Gas Flow Starts to Act	0.025	s
Moment when High-Speed Gas Flow Ends Its Action	0.065	s

This table is original and only data from Refs. [16] and [18] are used. The value of the response coefficient ranges from 0 to 1. When the response coefficient is 1, it means complete rebound (no loss of kinetic energy); when the response coefficient is 0, it means no rebound at all (complete loss of kinetic energy). In this paper, the reason for setting the response coefficient of particle–particle collision to 0.95 is to consider that the particle–particle collision is close to complete rebound, while the reason for setting the response coefficient of particle–wall collision to 0.31 is to consider that the particle–wall collision is close to complete non-rebound. When the spring coefficient in OpenFOAM is set to 1.5, the physical meaning is that the change in the response coefficient is non-linear. The value of the spring coefficient does not affect the calculation results since the response coefficient is a given value here, but it is a parameter that OpenFOAM requires to be set. Other parameters not stated as sources are geometric and computational control parameters, whose settings are based on the author's previous PBF-LB simulation study.[25]

Table III. Calculation Schemes for Analyzing Spatter Formation and Powder Bed Denudation

Calculation Scheme	Inlet Velocity of High-Speed Gas Flow (m/s)	Inlet Sizes of High-Speed Gas Flow (μm)
A1	(0, 0, 20)	90 × 90
A2	(0, 0, 30)	90 × 90
A3	(0, 0, 50)	90 × 90
A4	(0, 0, 30)	180 × 90
A5	(0, 0, 30)	90 × 180
A6	(0, 0, 30)	180 × 180

The metal vapor flow rate and area in the actual PBF-LB process are dynamically changing, and the six calculation schemes used herein are mainly used to analyze the effect of the velocity magnitude and size of the high-speed gas flow on the spatter behavior, and do not directly yield the real spatter behavior.

increased significantly [Figures 8(b), (c)]. Figure 7 gives the predicted results of the powder bed denudation zone for different calculation schemes. Combined with the data of the denudation zone width given in Figure 8(d), it is easy to know that the denudation zone width increased significantly when the inlet velocity or the inlet area increased. In summary, the spatter speed and the width of the powder bed denudation zone are mainly affected by the combination of the metal vapor jet speed and area, *i.e.,* the larger the metal vapor jet speed or area, the faster the spatter speed and the larger the width of the powder bed denudation; the number of spatters is closely related to the transverse dimension of the metal vapor action zone (the scanning direction is longitudinal), *i.e.,* the larger the transverse dimension of the metal vapor action zone, the larger the number of spatters.

B. *Effect of Protective Gas on Spatter Motion*

The paper then focuses on the effect of the protective gas on the spatter motion after the spatter has been formed. The parameters required for the calculation are consistent with Table II. Figure 9 shows the geometric and mesh models, where the forming cavity size is 100 × 5 × 50 mm, the powder bed size is 10 × 5 × 0.1 mm, the powder bed is 10 mm from the right-side wall, and the height of both the protective gas

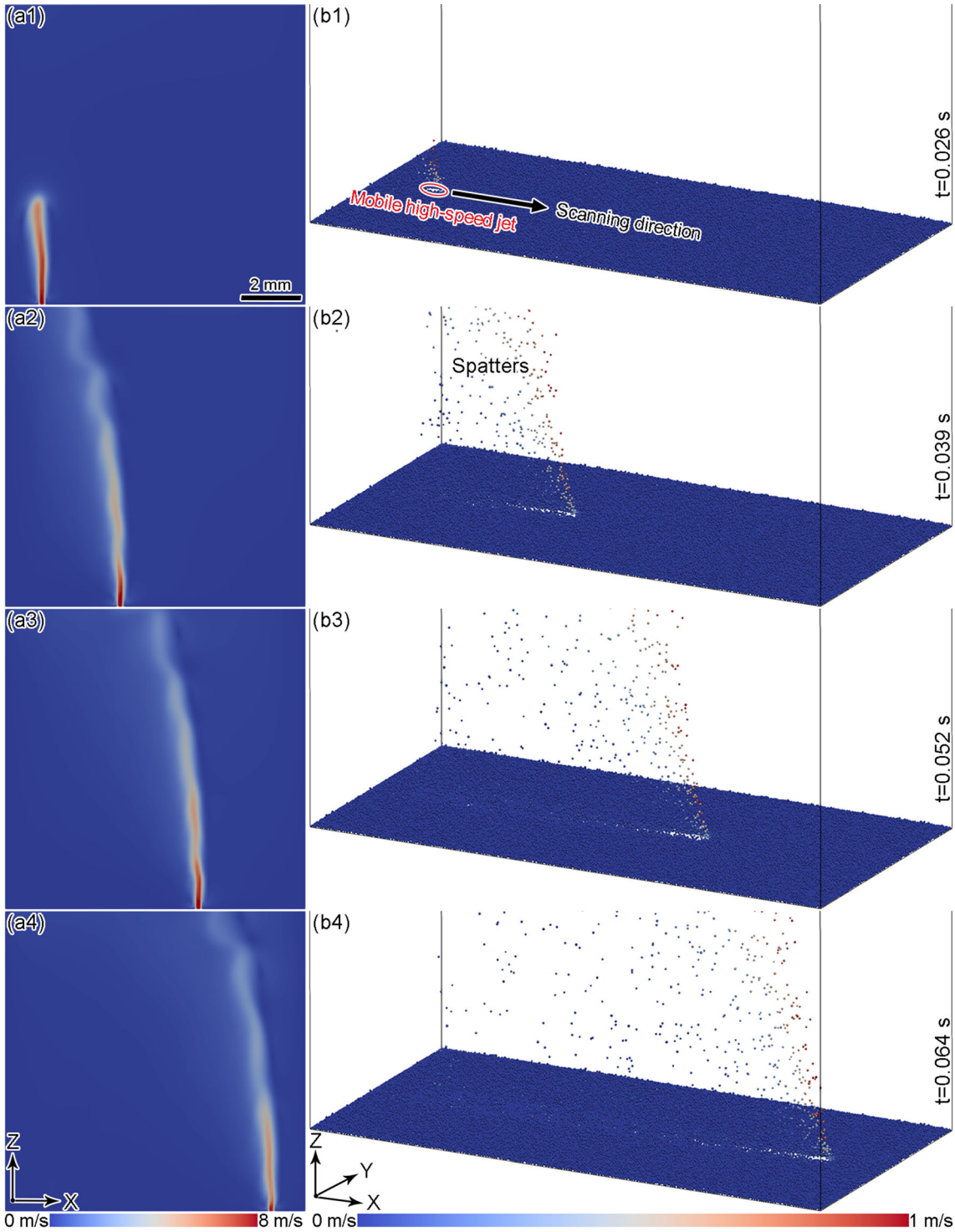

Fig. 3—Gas-phase velocity distribution of the Y-directional mid-section (*a1* to *a4*) and 3D spatter distribution (*b1* to *b4*) at different moments for calculation scheme A2.

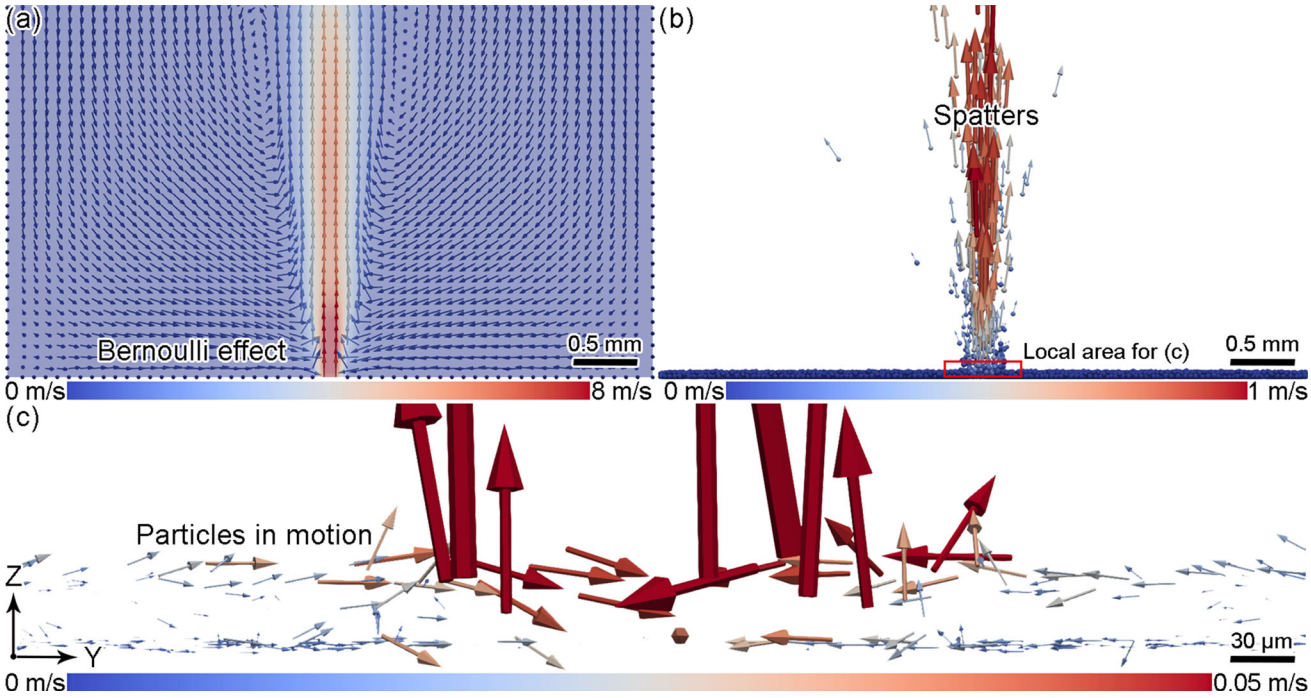

Fig. 4—X-directional cross-sectional gas-phase flow velocity distribution (*a*), spatter velocity distribution (*b*) and local particles velocity distribution (*c*) at the moment of t = 0.03 s for calculation scheme A2.

inlet and outlet is 15 mm, and both are 10 mm from the bottom wall [Figure 9(a)]. On the basis of ensuring the accuracy of calculation, in order to reduce the number of meshes as much as possible, this paper divided the non-uniform mesh with the help of the *blockMesh* function that comes with OpenFOAM, *i.e.,* the X- and Y-directional mesh sizes of the calculation domain were 100 μm, and the Z-directional mesh size transitioned from 100 to 312.5 μm according to certain rules, and the total number of nodes finally obtained was 13,079,358, and the total number of cells was 12,760,000 [Figure 9(b)]. The high-speed gas flow inlet velocity was (0, 0, 30) m/s, the high-speed gas flow inlet size was 100 × 100 μm, and the total calculation time was 0.25 second. In addition, parallel calculations were carried out with the help of OpenMPI and the computational mesh was manually partitioned in order to assign as many cores as possible to the particle calculations. In order to analyze the effect of the protective gas on the spatter motion, simulation studies were carried out as shown in Table IV.

Figure 10 gives the gas-phase flow velocity and spatter distributions at different moments for calculated scheme B1. From the calculation results, it can be seen that the metal particles were ejected under the action of high-speed gas flow to form the spatter. Subsequently, due to the obvious flow of protective gas above the powder bed, the spatter was deflected significantly under the drag effect of the protective gas flow, *i.e.,* the protective gas flow showed an obvious spatter removal effect. The different results of the spatter motion in the case of calculation scheme B1 are given in Figure 11. Among them, the destination of the splatter can be divided into three main scenarios: the first scenario is due to the low initial velocity of the spatter and the limited movement height, thus being less influenced by the protective gas flow, which tends to fall into the powder bed or the substrate [Figures 11(b1), (b2)]; the second and third scenarios are both due to the high initial velocity of the spatter, which is more influenced by the protective gas flow and thus being removed directly *via* the protective gas outlet [Figures 11(c1), (c2)], or collision with the side wall [Figures 11(d1), (d2)]. It can be seen that combining the spatter formation with the protective gas flow and carrying out the calculation of the spatter-protective gas flow coupling can provide guidance for optimizing the spatter removal measures.

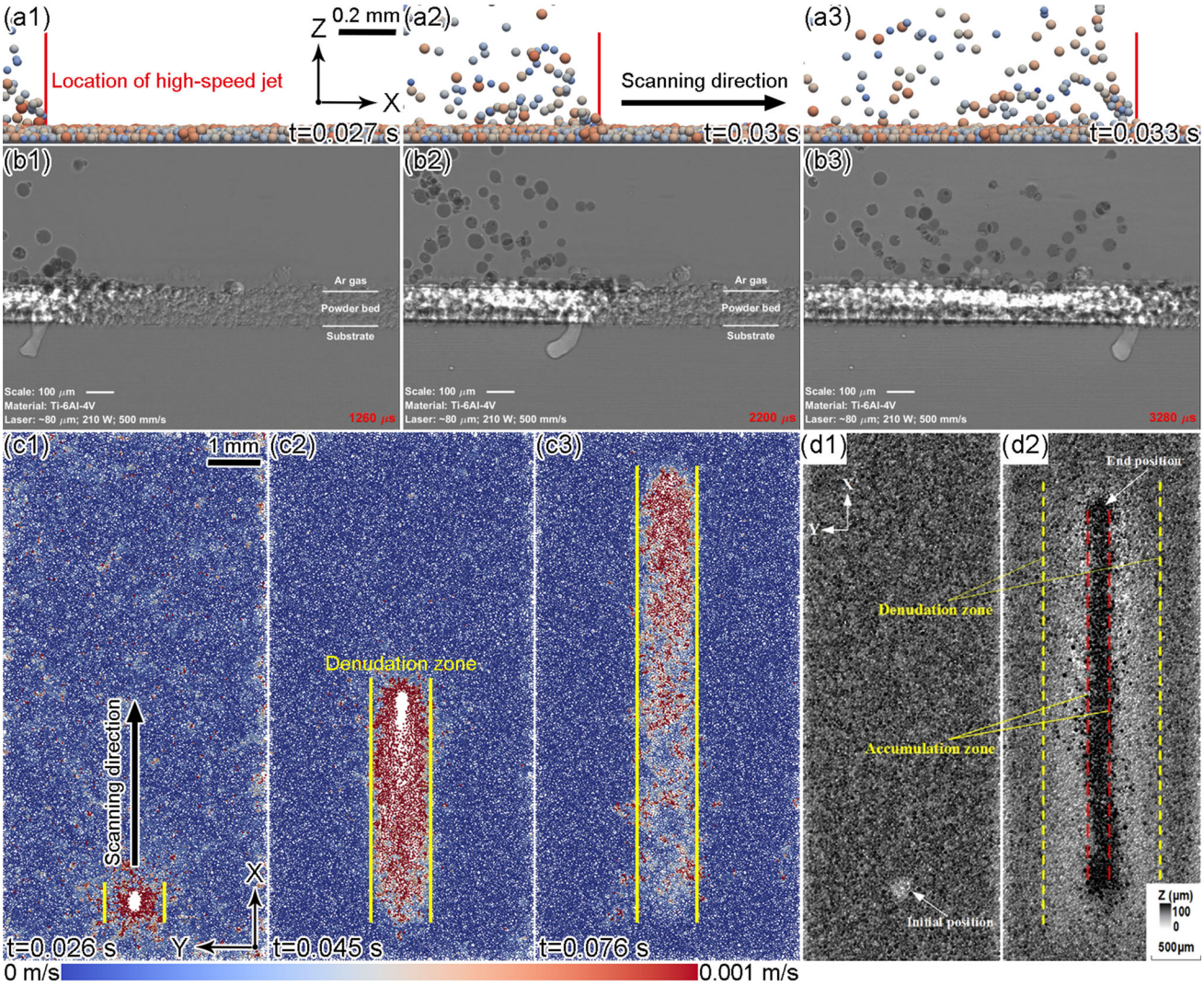

Fig. 5—Simulation and experimental comparison of spatter and powder bed denudation: (*a1* ~ *a3*) spatter distribution at different moments for calculation scheme A2; (*b1* ~ *b3*) experimentally obtained spatter distribution at different moments[27]; (*c1* ~ *c3*) powder bed denudation area at different moments for calculation scheme A2; (*d1* ~ *d2*) experimentally obtained powder bed denudation area[17] (Note: Parts b1, b2, and b3 are reprinted from reference,[27] under the terms of the Creative Commons CC BY 4.0 license; parts d1 and d2 are reprinted with permission from reference[17]).

The calculation results for different protective gas inlet velocities are given in Figures 12, 13, 14. From the comparison results, it can be seen that as the inlet velocity of the protective gas gradually decreased, the protective gas flow rate gradually decreased [Figure 12(a1) to (a3)], and then the influence of the protective gas flow on the spatter gradually decreased, which made the movement distance of the spatter in the X-direction significantly shorten [Figures 12(b1), (b3)]. Figure 13 gives the final distribution of particles and the spatter motion trajectory under different calculation schemes. From the calculation results, it can be seen that when the protective gas inlet velocity was large, a considerable part of the spatter would eventually be

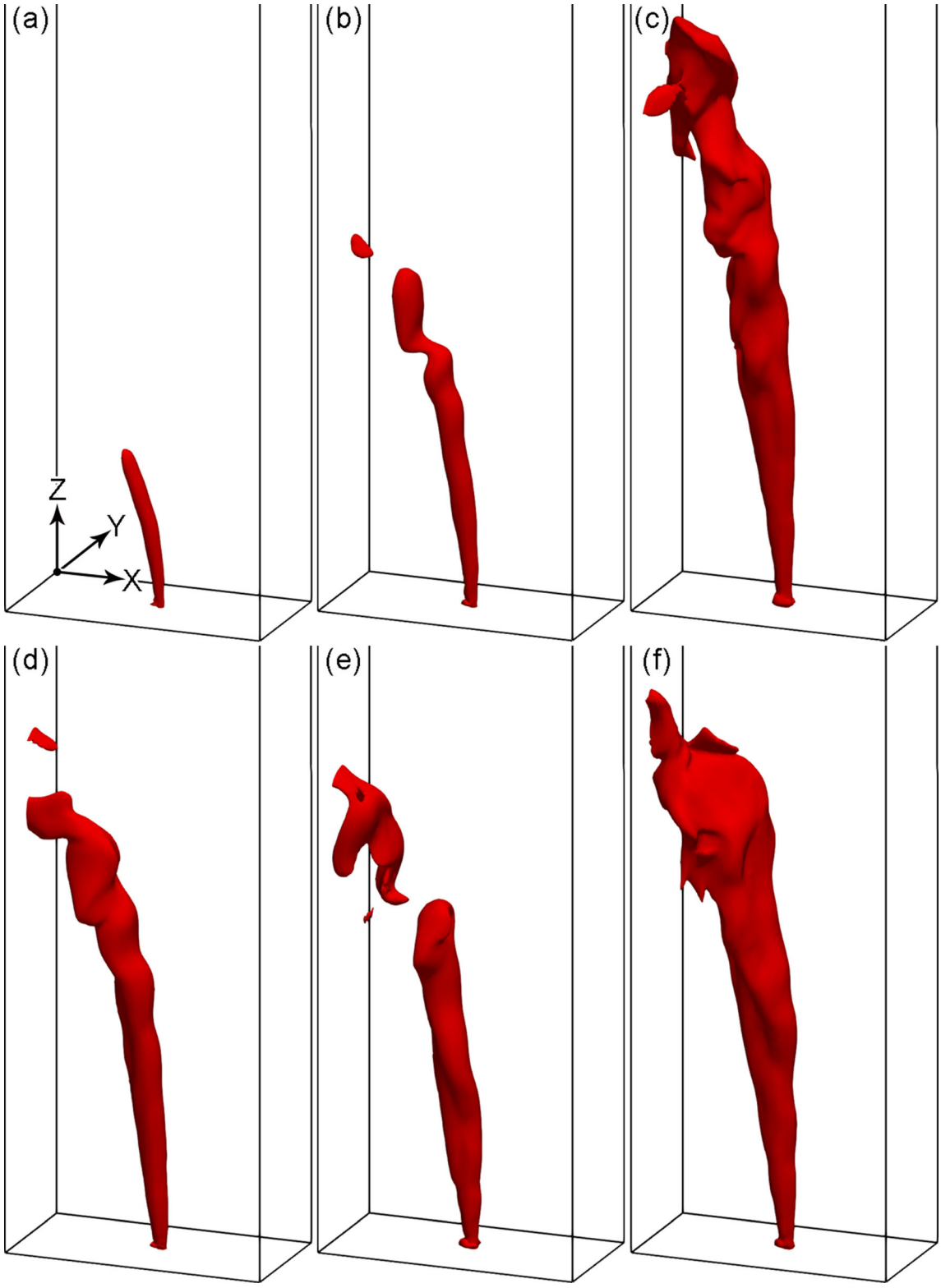

Fig. 6—High-speed jet zone at the moment of t = 0.045 s for different calculation schemes (equivalent surface with gas-phase rate of 1 m/s): (*a*) scheme A1; (*b*) scheme A2; (*c*) scheme A3; (*d*) scheme A4; (*e*) scheme A5; (*f*) scheme A6.

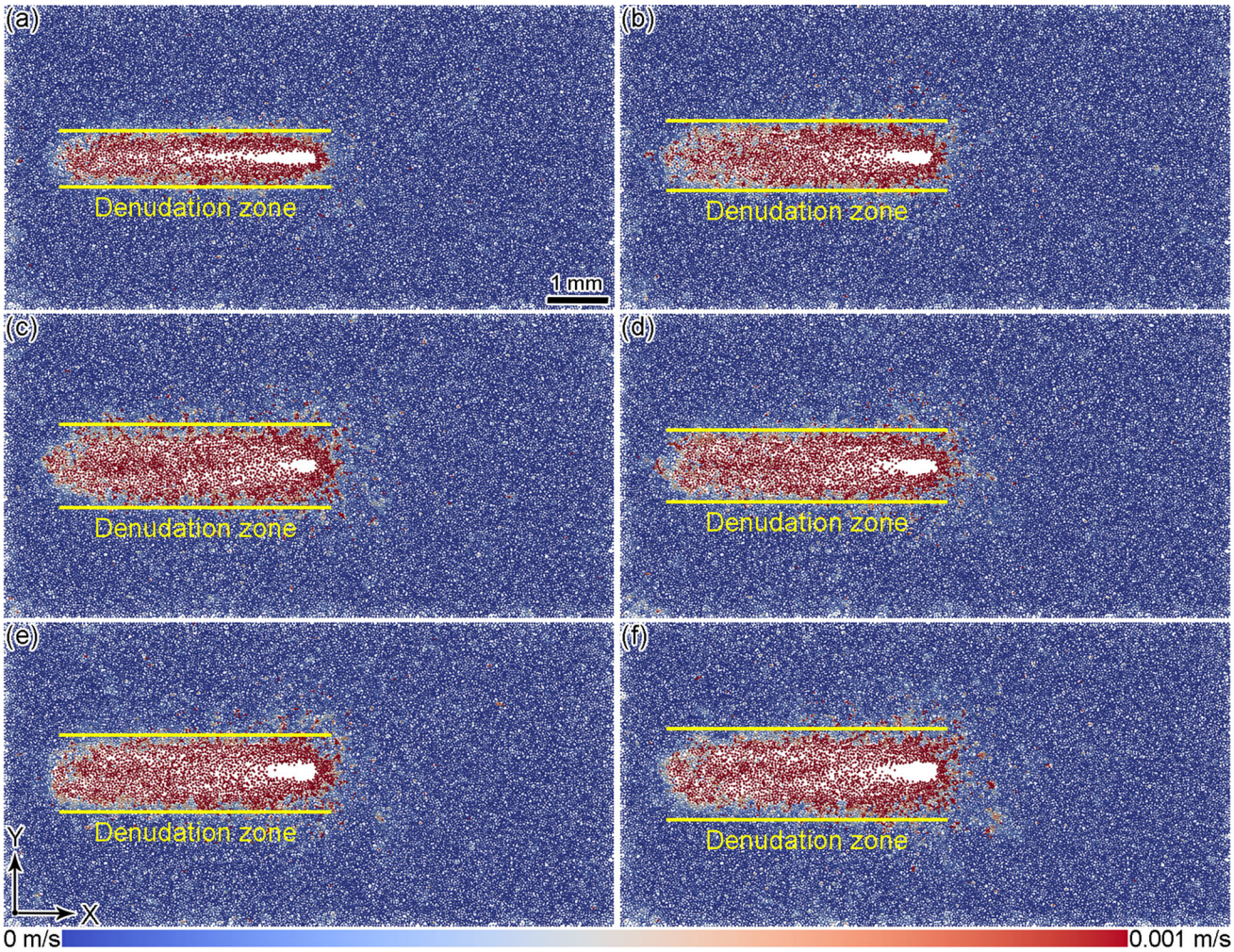

Fig. 7—Powder bed denudation zone at the moment of t = 0.045 s for different calculation schemes: (*a*) scheme A1; (*b*) scheme A2; (*c*) scheme A3; (*d*) scheme A4; (*e*) scheme A5; (*f*) scheme A6.

removed *via* the protective gas outlet or collide with the side wall, which in turn made a large amount of spatter eventually accumulate near the left wall of the forming cavity [Figures 13(a1), (b1)]. Figure 14(a) illustrates this phenomenon quantitatively, while Figure 14(c) demonstrates that more spatters were removed *via* the protective gas outlet at higher protective gas inlet velocities. When the protective gas inlet velocity was small, almost all of the spatter fell into the powder bed or substrate [Figures 13(a3), (b3)]. In addition, Figure 14(b) illustrates that the spatter eventually moved a limited distance in the Y-direction and showed a clear pattern of clustering near the scanning path. Figure 14(d) illustrates that when the protective gas inlet velocity was larger, the more complex the protective gas flow field inside the forming cavity was, the more the local vortex area formed even brought the spatter into the front of the scanning zone. In summary, the protective

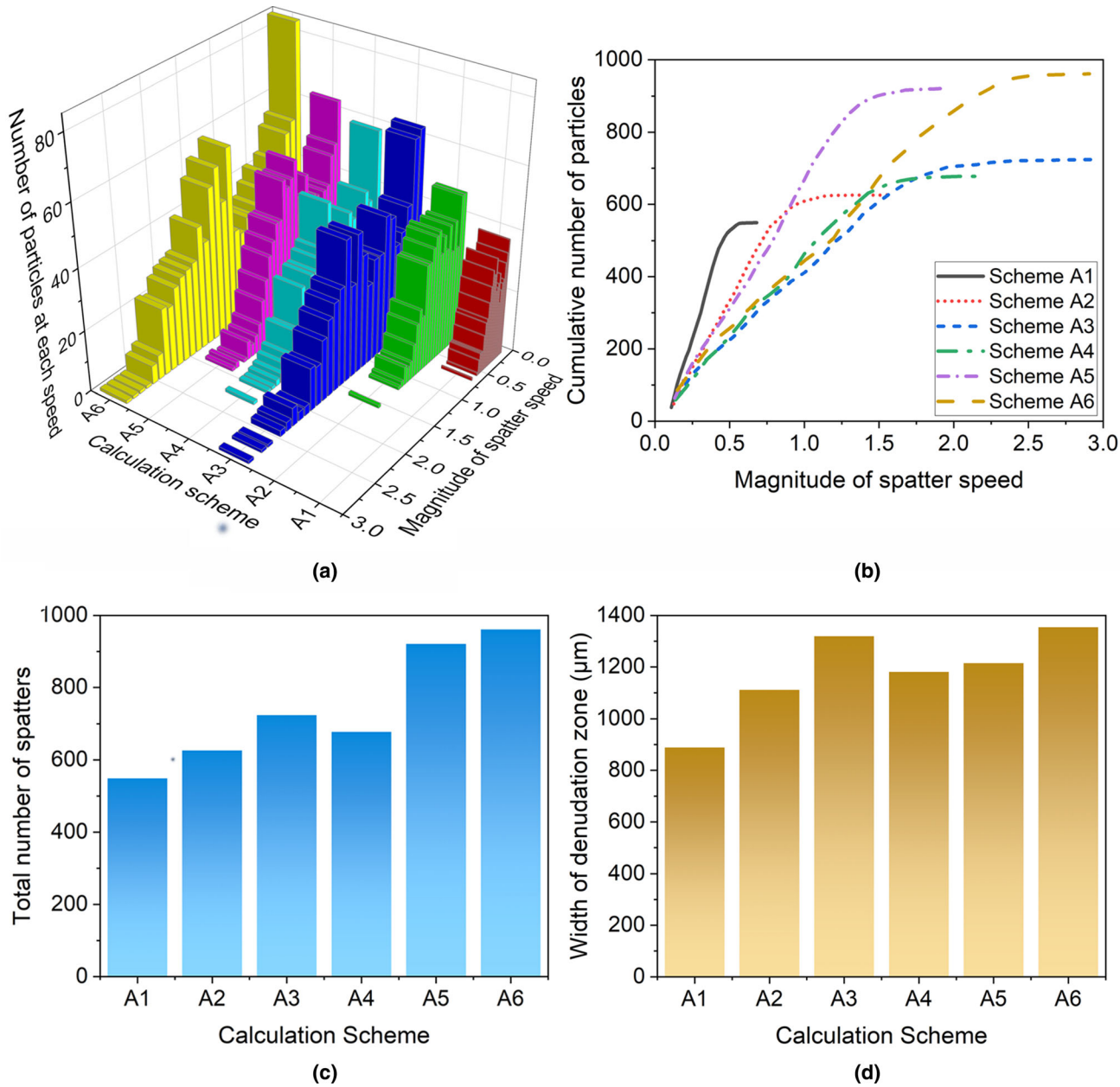

Fig. 8—Comparison of spatter and powder bed denudation data for different calculation schemes: (*a*) "spatter velocity-particles number" histogram; (*b*) "spatter velocity-accumulated particles number" curve; (*c*) total number of spatters; (*d*) width of powder bed denudation zone.

gas flow velocity has a significant effect on the spatter motion. The longitudinal (*i.e.,* scanning direction) movement distance of the spatter is significantly larger for larger protective gas flow velocities, and almost all of the spatter falls into the powder bed or substrate for smaller protective gas flow velocities.

IV. CONCLUSIONS

(1) In this paper, Eulerian–Lagrangian numerical simulations based on OpenFOAM, an open-source CFD code, were carried out to investigate

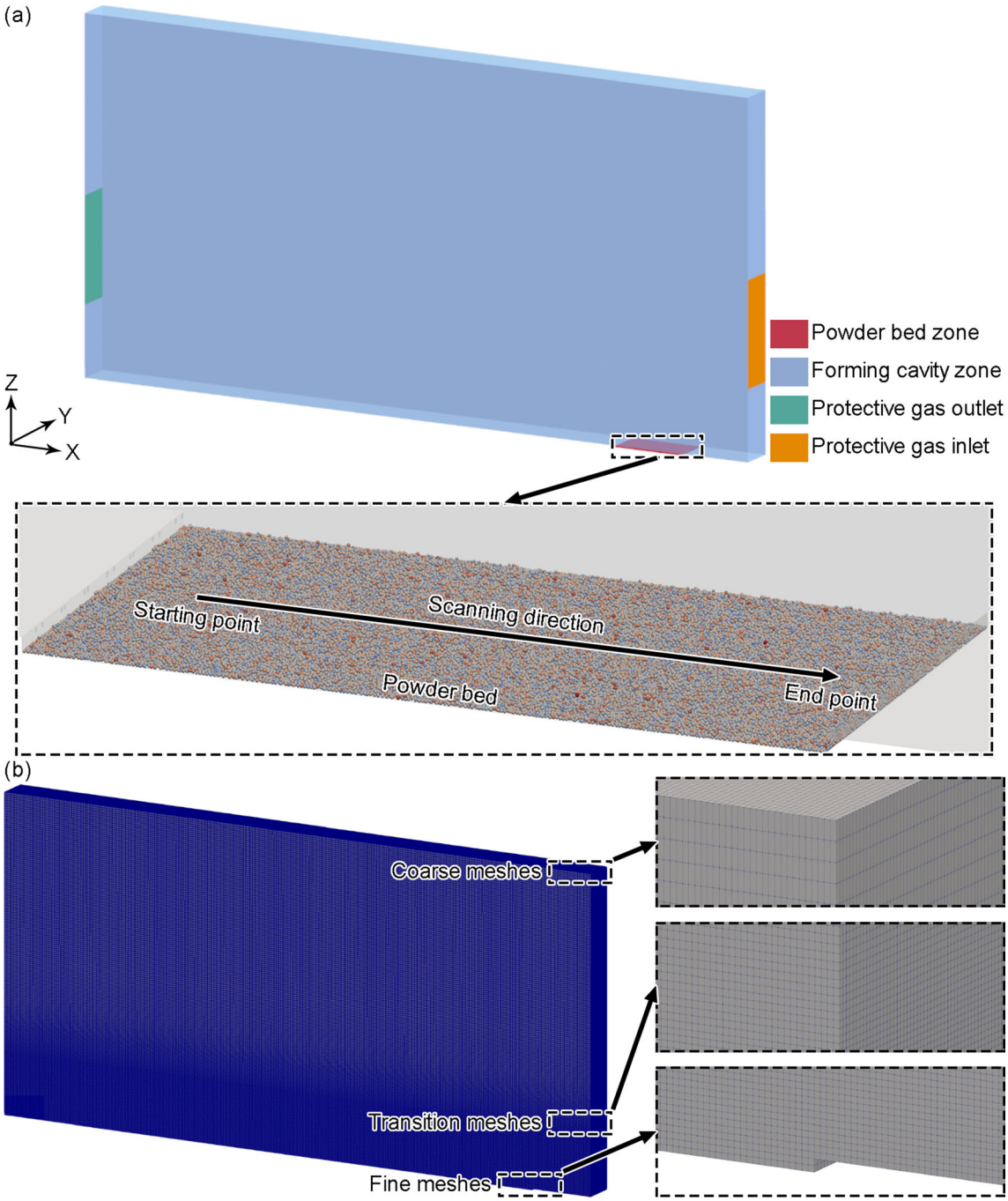

Fig. 9—Geometric model and mesh model: (*a*) geometric model; (*b*) mesh model.

Table IV. Calculation Schemes for Analyzing the Effect of Protective Gas on Spatter Motion

Calculation Scheme	Protective Gas Inlet Velocity (m/s)
B1	(− 1.5, 0, 0)
B2	(− 1.0, 0, 0)
B3	(− 0.5, 0, 0)

The actual PBF-LB process in which the protective gas inlet velocity is dynamically changing, and the three calculation schemes used herein are mainly used to analyze the effect of the protective gas inlet velocity magnitude on the spatter behavior and do not directly derive the real spatter behavior.

the powder bed denudation and spatter behaviors during PBF-LB forming process. The Eulerian model was used to describe the gas-phase motion, which took into account the effect of particles on the gas-phase flow and applied a turbulence model; the Lagrangian model was used to describe the particle motion, which took into account fluid drag force, gravity, buoyancy, non-uniform pressure distribution, additional mass forces, and particle–particle collisions.

(2) For the effect of metal vapor jet speed and jet area on the spatter formation and powder bed

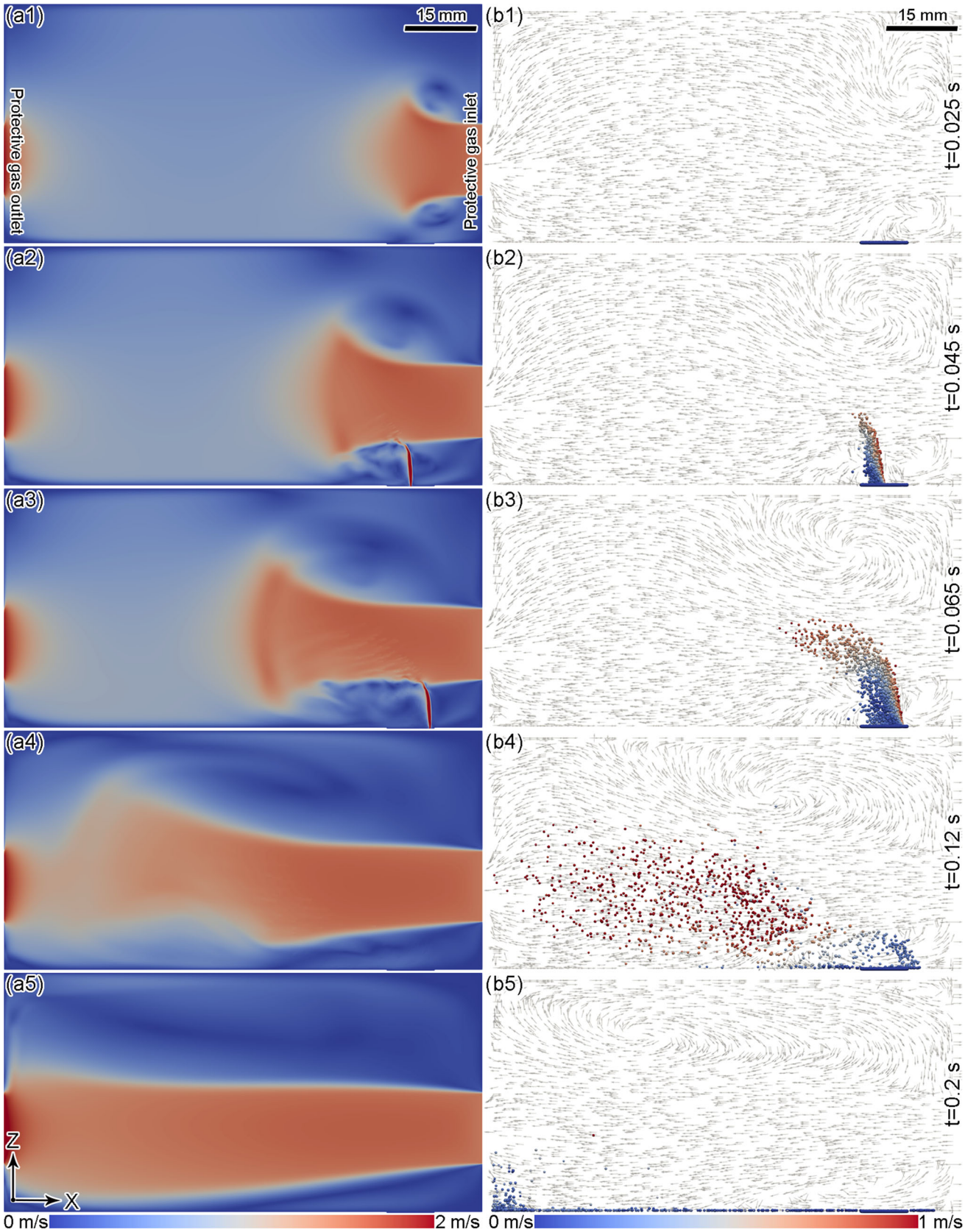

Fig. 10—Gas-phase flow velocity distributions (*a1* to *a5*) and spatter distributions (*b1* to *b5*) of the Y-directional mid-section at different moments for calculation scheme B1 (Note: The particles were magnified 15 times during post-processing to clearly show them).

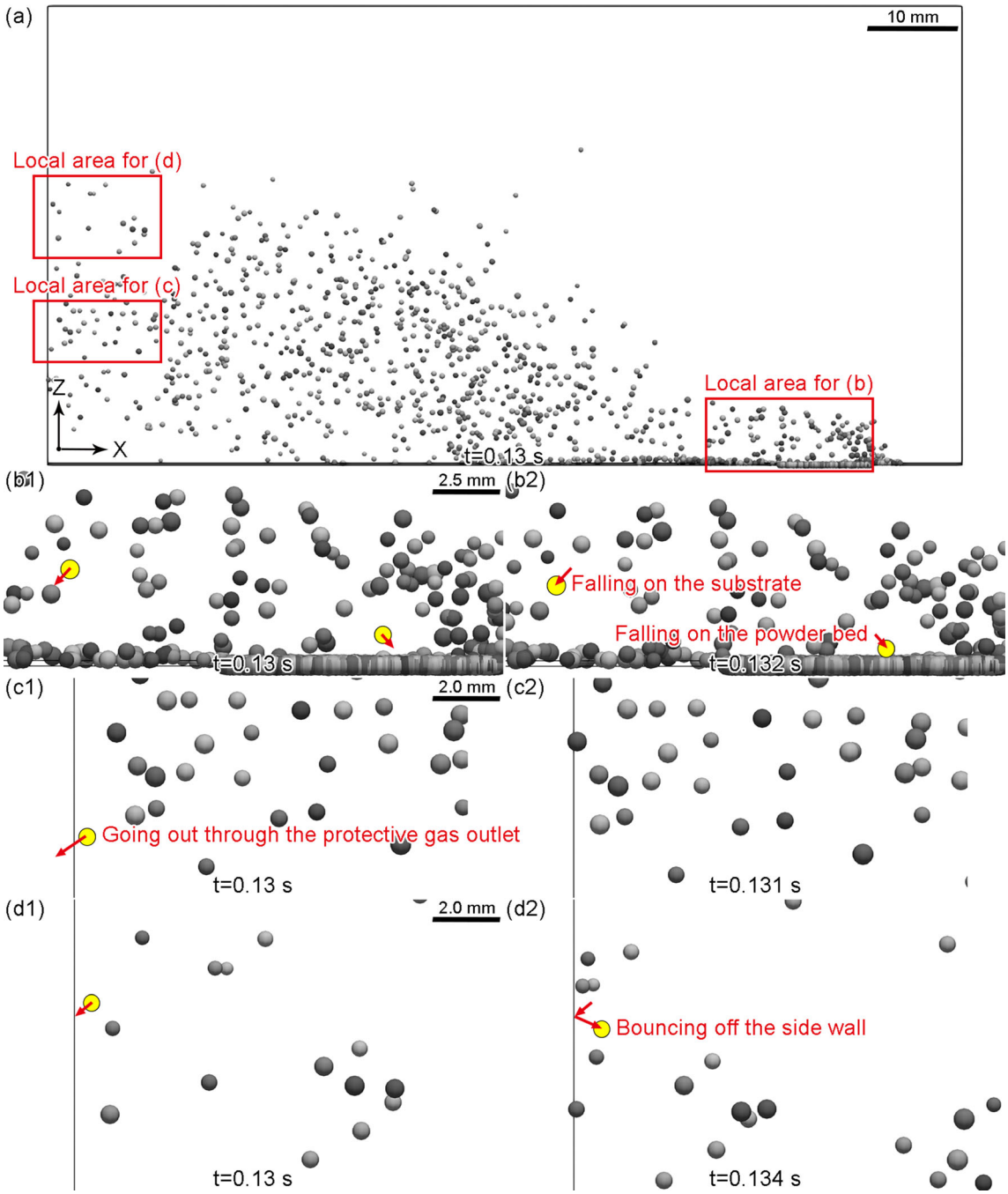

Fig. 11—Different results of the spatter motion for calculation scheme B1: (*a*) spatter distribution at the moment of t = 0.13 s; (*b1*, *b2*) spatter falling into the powder bed or substrate; (*c1*, *c2*) spatter removed *via* the protective gas outlet; (*d1*, *d2*) spatter bouncing off the side wall (Note: The particles were magnified 15 times during post-processing to clearly show them).

denudation, it was found that the larger the metal vapor jet speed or area, the faster the spatter speed and the larger the width of the powder bed denudation zone; the larger the transverse dimension of the metal vapor action zone (scanning direction is longitudinal), the larger the number of spatter.

(3) For the effect of protective gas flow velocity on spatter motion, it was found that the longitudinal movement distance of spatter was significantly

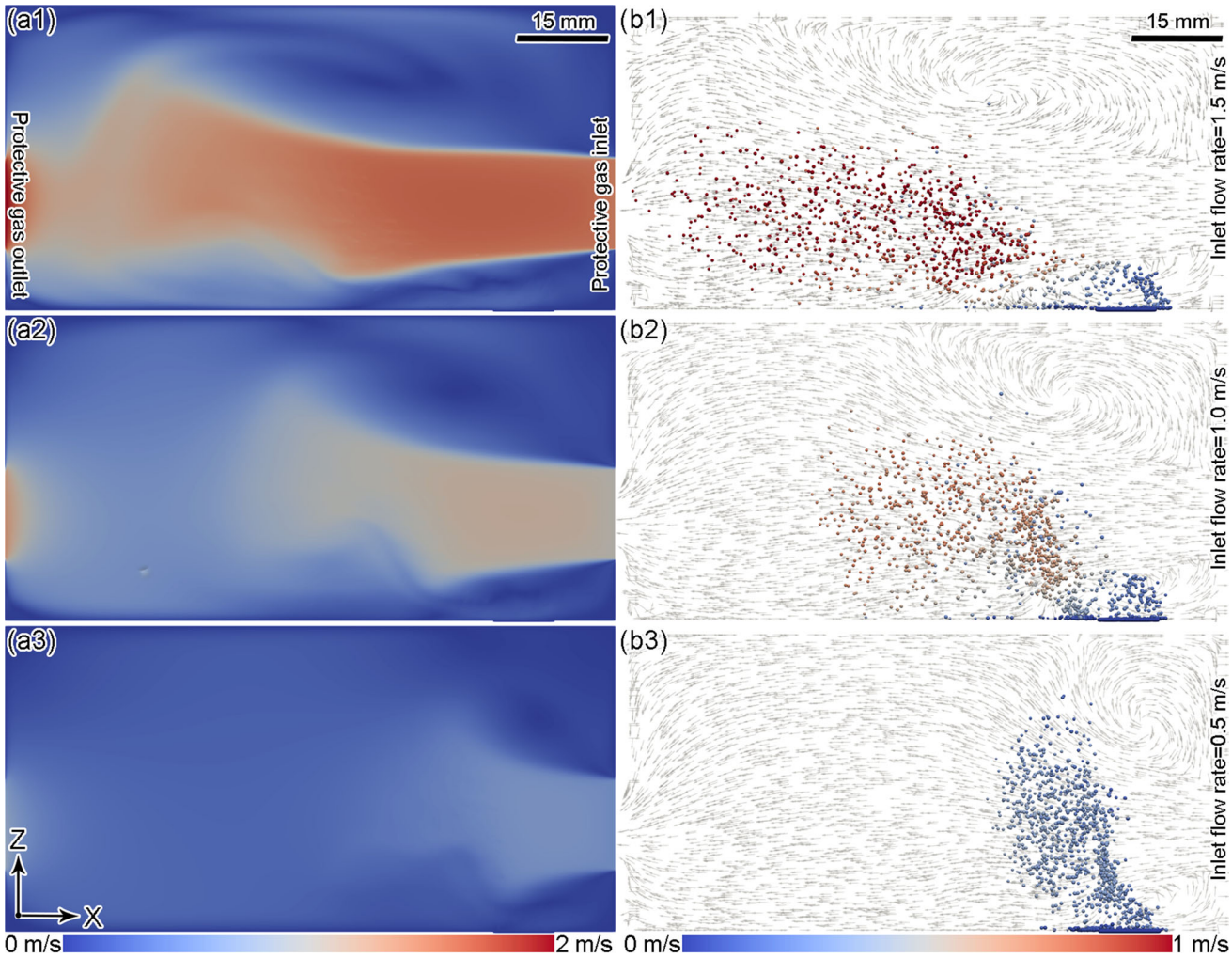

Fig. 12—Gas-phase flow velocity distributions in the Y-directional mid-section (*a1* to *a3*) and spatters distributions (*b1* to *b3*) at the moment of t = 0.12 s for different protective gas inlet flow velocities (Note: The particles were magnified 15 times during post-processing to clearly show them).

larger for larger protective gas flow velocities, and almost all splash fell into the powder bed or substrate for smaller protective gas flow velocities.

(4) As a pre-study of PBF-LB spatter behavior, certain simplifications and assumptions were adopted in this paper, such as imposing a high-speed inlet boundary instead of metal vapor and not considering droplet spatter. In fact, the PBF-LB phase transformation process involves the coupling between metal solid phase, metal liquid phase, metal vapor phase, metal particle phase, and protective gas phase, and the direct prediction of the complex kinetic behavior of these five phases is one of the main difficulties and one of the main development directions in the current PBF-LB numerical simulation research. Since the multiphase coupling behavior is not directly predicted, the formation of metal vapor phase cannot be directly predicted here, and the gas-phase inlet velocity can only be set based on the experiment. Since the accuracy of current

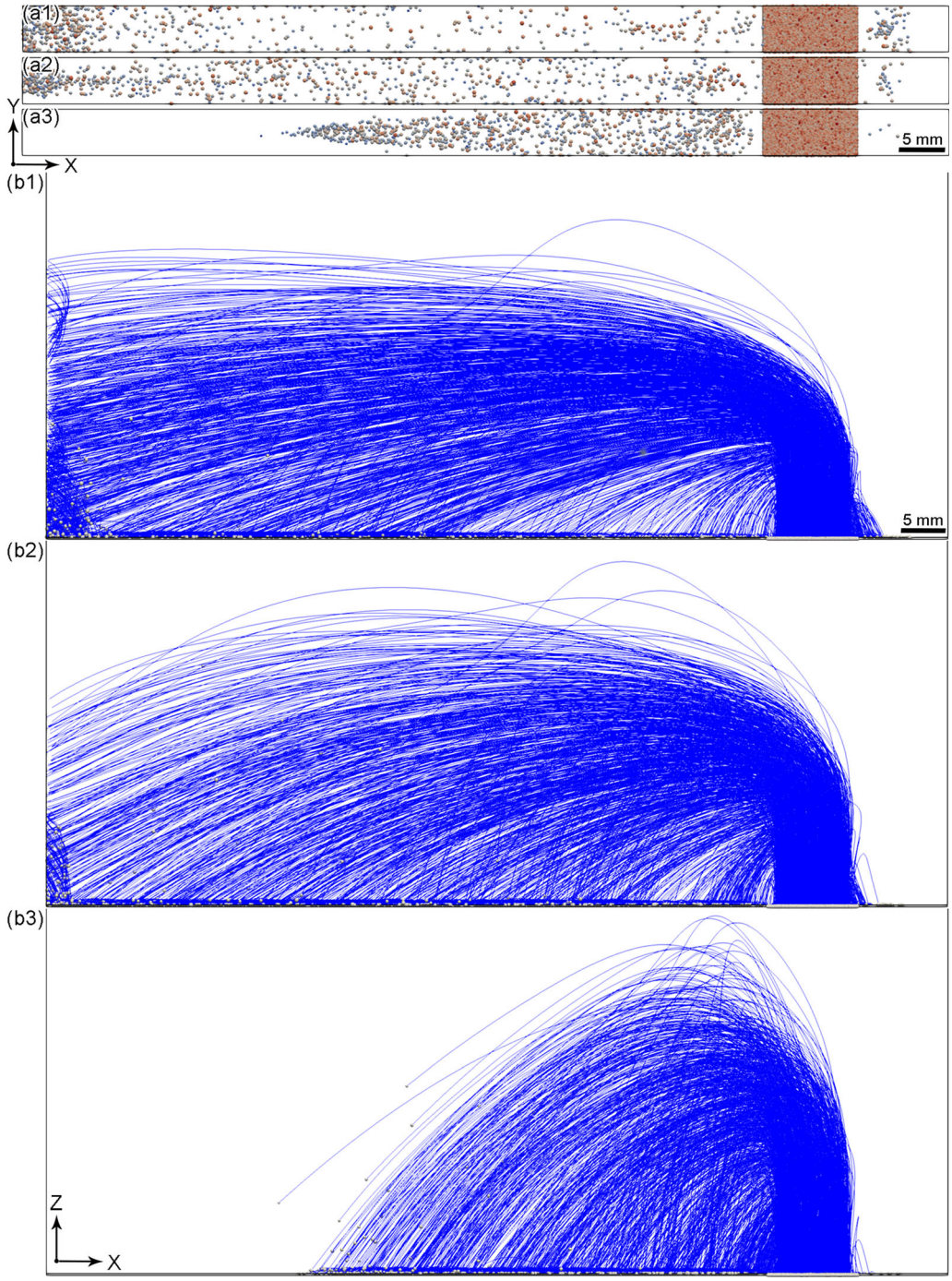

Fig. 13—Final particle distributions (*a1* to *a3*) and spatter motion trajectories (*b1* to *b3*) for different calculation schemes: (*a1*, *b1*) scheme B1; (*a2*, *b2*) scheme B2; (*a3*, *b3*) scheme B3 (Note: The particles were magnified 10 times during post-processing to clearly show them).

experimental determination of metal vapor flow speed is low, and the formation of metal vapor during PBF-LB-forming process is dynamic, which makes the artificial setting of inlet velocity reduce the accuracy of prediction results; therefore, the melting, solidification. and vaporization phase transformation processes need to be considered in the next study to reveal the generation and motion law of spatter (powder spatter and droplet spatter) in a more realistic way. In

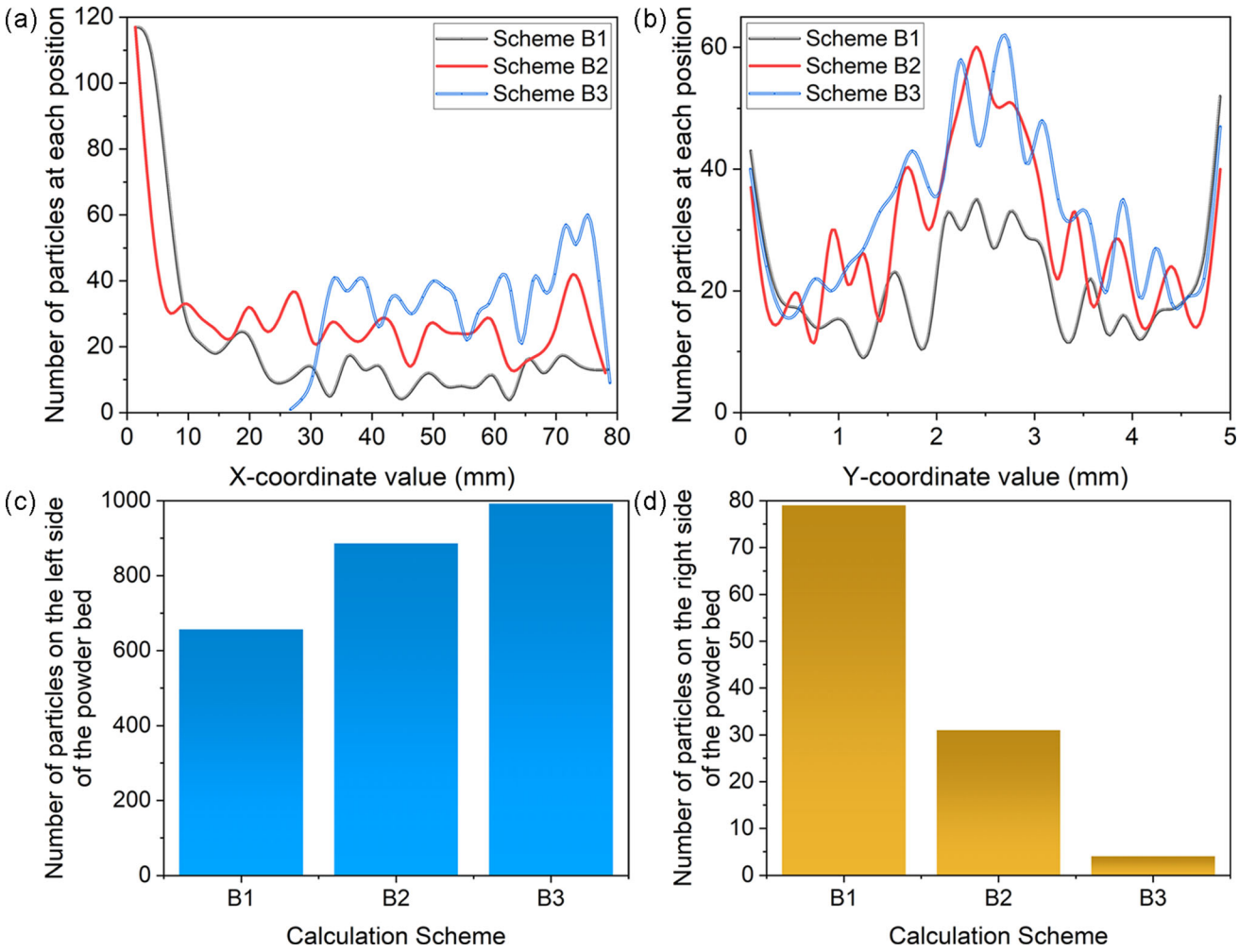

Fig. 14—Comparison of the final particle distribution data for different calculation schemes: (*a*) "X coordinate-particle number" curve of particles finally located on the left side of the powder bed; (*b*) "Y coordinate-particle number" curve of particles finally located on the left side of the powder bed; (*c*) number of particles finally located on the left side of the powder bed; (*d*) number of particles finally located on the right side of the powder bed.

addition, conducting PBF-LB experiments under different process conditions and comparing and analyzing the experimental and simulation results of the final distribution of spatter to verify the accuracy of PBF-LB spatter prediction are also one of the focuses of the subsequent research.

ACKNOWLEDGMENTS

This work was supported by the Basic and Applied Basic Research Project of Guangzhou Basic Research Program (no. 202102020724), the Natural Science Foundation of Guangdong Province (no. 2019A1515012040), and the Fast Support Project (No. 80923010304).

CONFLICT OF INTEREST

On behalf of all authors, the corresponding author states that there is no conflict of interest.

REFERENCES

1. E.M. Sefene: *Manuf. Syst.*, 2022, vol. 63, pp. 250–74.
2. M.T. Andani, R. Dehghani, M.R. Karamooz-Ravari, R. Mirzaeifar, and J. Ni: *Mater. Design*, 2017, vol. 131, pp. 460–69.
3. Y. Liu, Y.Q. Yang, S.Z. Mai, D. Wang, and C.H. Song: *Mater. Design*, 2015, vol. 87, pp. 797–806.
4. S. Ly, A.M. Rubenchik, S.A. Khairallah, G. Guss, and M.J. Matthews: *Sci. Rep.*, 2017, vol. 7, p. 4085.
5. M.J. Matthews, G. Guss, S.A. Khairallah, A.M. Rubenchik, P.J. Depond, and W.E. King: *Acta Mater.*, 2016, vol. 114, pp. 33–42.
6. D. Wang, W.H. Dou, Y.H. Ou, Y.Q. Yang, C.L. Tan, and Y.J. Zhang: *J. Mater. Res. Technol.*, 2021, vol. 12, pp. 1051–64.

7. L.I. Escano, N.D. Parab, L.H. Xiong, Q.L. Guo, C. Zhao, T. Sun, and L.Y. Chen: *Synchrotron Radiation News*, 2019, vol. 32, pp. 9–13.
8. S.Y. Luo, X.Q. Ma, J. Xu, M.L. Li, and L.C. Cao: *Sensors*, 2021, vol. 21, p. 7179.
9. M. Slodczyk, A. Ilin, T. Kiedrowski, T. Bareth, and V. Ploshikhin: *Mater. Design*, 2021, vol. 212, p. 110206.
10. W.H. Zhang, H.L. Ma, Q. Zhang, and S.Q. Fan: *Mater. Design*, 2022, vol. 213, p. 110301.
11. C. Pauzon, B. Hoppe, T. Pichler, S.D.-L. Goff, P. Forêt, T. Nguyen, and E. Hryha: *CIRP J. Manuf. Sci. Technol.*, 2021, vol. 35, pp. 371–78.
12. Z.A. Young, Q.L. Guo, N.D. Parab, C. Zhao, M.L. Qu, L.I. Escano, K. Fezzaa, W. Everhart, T. Sun, and L.Y. Chen: *Addit. Manuf.*, 2020, vol. 36, 101438.
13. T. Tran-Le, J. X. Wang, M. Byron, S. Lynch, R. Kunz: *Proceedings of the ASME 2021*, 2021, DOI: https://doi.org/10.1115/IMECE2021-69550.
14. M.L. Qu, Q.L. Guo, L.I. Escano, A. Nabaa, S.M.H. Hojjatzadeh, Z.A. Young, and L.Y. Chen: *Nat. Commun.*, 2022, vol. 13, p. 1079.
15. R. Kasper, J. Turnow, and N. Kornev: *Int. J. Heat Fluid Fl.*, 2019, vol. 79, p. 108462.
16. H. Chen, Y.J. Zhang, A. Giam, and W.T. Yan: *Addit. Manuf.*, 2022, vol. 52, p. 102645.
17. H. Chen and W.Y. Yan: *Acta Mater.*, 2020, vol. 196, pp. 154–67.
18. C.-Y. Chien, T.-N. Le, Z.-H. Lin, and Y.-L. Lo: *Mater. Design*, 2021, vol. 210, p. 110107.
19. T. Yu and J.D. Zhao: *Comput. Method. Appl. Mater.*, 2021, vol. 377, p. 113707.
20. X.B. Zhang, B. Cheng, and C. Tuffile: *Addit. Manuf.*, 2020, vol. 32, p. 101049.
21. A.B. Anwar, I.H. Ibrahim, and Q.-C. Pham: *Powder Technol.*, 2019, vol. 352, pp. 103–16.
22. J. Jakumeit, G.Y. Zheng, R. Laqua, S.J. Clark, J. Zielinski, J.H. Schleifenbaum, and P.D. Lee: *Addit. Manuf.*, 2021, vol. 47, p. 102332.
23. R. Kasper, J. Turnow, and N. Kornev: *Int. J. Heat Mass Tran.*, 2017, vol. 115, pp. 932–45.
24. L. Cao: *Int. J. Adv. Manuf. Tech.*, 2019, vol. 105, pp. 2253–69.
25. L. Cao and W. Guan: *Int. J. Adv. Manuf. Technol.*, 2021, vol. 114, pp. 2141–57.
26. C. Kloss, C. Goniva, A. Hager, S. Amberger, and S. Pirker: *Prog. Comput. Fluid Dyn.*, 2012, vol. 12, pp. 140–52.
27. C. Zhao, Q.L. Guo, X.X. Li, N. Parab, K. Fezzaa, W.D. Tan, L.Y. Chen, and T. Sun: *Phys. Rev. X*, 2019, vol. 9, 021052.

Publisher's Note Springer Nature remains neutral with regard to jurisdictional claims in published maps and institutional affiliations.

Springer Nature or its licensor (e.g. a society or other partner) holds exclusive rights to this article under a publishing agreement with the author(s) or other rightsholder(s); author self-archiving of the accepted manuscript version of this article is solely governed by the terms of such publishing agreement and applicable law.